Biointerface Research in Applied Chemistry
Open-Access Journal (ISSN: 2069-5837)

Article
Volume 14, Issue 6, 2024, 135
https://doi.org/10.33263/BRIAC146.135

In Silico Assessment of the ADMET Properties of 7-Hydroxymitragynine and its Interaction with Human Serum Albumin and α_1-Acid Glycoprotein

Khairul Azreena Bakar [1], Su Datt Lam [2,3,4], Chen Fei Low [3,5], Shevin Rizal Feroz [1,3,*]

1 Department of Biological Sciences and Biotechnology, Faculty of Science and Technology, Universiti Kebangsaan Malaysia, 43600 Bangi, Selangor, Malaysia; p109997@siswa.ukm.edu.my (K.A.B); shevin@ukm.edu.my (S.R.F);
2 Department of Applied Physics, Faculty of Science and Technology, Universiti Kebangsaan Malaysia, 43600 Bangi, Selangor, Malaysia; sudatt@ukm.edu.my (L.S.D);
3 Structural Biology and Protein Engineering Group, Universiti Kebangsaan Malaysia, 43600, Bangi, Selangor, Malaysia; (L.S.D); low@ukm.edu.my (L.C.F); (S.R.F);
4 Center for Global Health Research (CGHR), Saveetha Medical College, Saveetha Institute of Medical and Technical Sciences (SIMATS), Saveetha University, Chennai, India (L.S.D);
5 Institute of Systems Biology, Universiti Kebangsaan Malaysia, 43600 Bangi, Selangor, Malaysia; (L.C.F);
* Correspondence: shevin@ukm.edu.my (S.R.F);

Scopus Author ID 55251086800
Received: date; Accepted: date; Published: date

Abstract: *Mitragyna speciosa* (kratom) is a psychoactive plant native to Southeast Asia that is traditionally used for pain relief, increased physical endurance, and as a muscle relaxant. Its most potent alkaloid, 7-hydroxymitragynine (7-OH-MTG), acts on the μ-opioid receptor, providing analgesic effects. Assessment of its drug-likeness and ADMET properties indicates the suitability of 7-OH-MTG as a drug with favorable pharmacokinetic profile. Further, characterization of its interaction with plasma transport proteins such as human serum albumin (HSA) and α1-acid glycoprotein (AAG) is vital for assessing its therapeutic potential. Molecular docking suggests preferential binding of 7-OH-MTG to site III on subdomain IB of HSA and the central binding pocket of both variants F1*S and A of AAG. The involvement of various hydrophobic interactions (alkyl, pi-alkyl, pi-pi), hydrogen bonds, and van der Waals forces are suggested in stabilizing the 7-OH-MTG–protein complexes. MD simulation results supported the overall stable nature of the binding of 7-OH-MTG to both proteins based on several parameters, including root-mean-square deviation (RMSD), total energy, root-mean-square fluctuation (RMSF), radius of gyration (Rg), and solvent accessible surface area (SASA). These findings have clear significance in the development of potential therapeutic agents derived from kratom.

Keywords: kratom; 7-hydroxymitragynine; human serum albumin; α_1-acid glycoprotein; ligand-protein interaction; molecular docking; molecular dynamics.

1. Introduction

Mitragyna speciosa, commonly known as kratom, is a psychoactive plant found in several regions of Southeast Asia where it is used traditionally for pain relief and treating common ailments, including coughs and fever [1]. Kratom is valued for its medicinal properties, including antinociceptive and antidepressant effects [1, 2]. Local laborers often consume kratom leaves as a stimulant to boost energy and endurance [3]. 7-Hydroxymitragynine (7-OH-MTG) (Figure 1) is a minor alkaloid of kratom that, although it makes up only ~2% of the total alkaloid content of the plant, acts on the μ-opioid receptor to

elicit analgesic effects that are approximately 13 and 46 times more potent than morphine and mitragynine (MTG), respectively [4, 5]. Thus, despite its lower abundance compared to MTG, 7-OH-MTG contributes significantly to the analgesic, sedative, and potentially addictive properties of kratom [6].

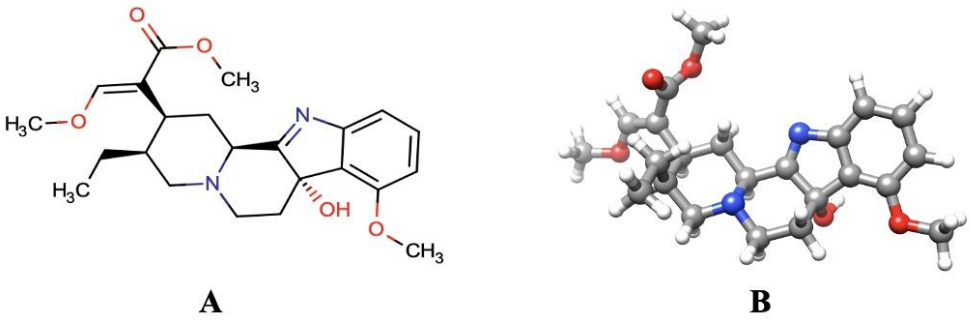

Figure 1. (A) 2D; **(B)** 3D structures of 7-OH-MTG.

A drug's absorption, distribution, metabolism, excretion, stability, and toxicity are greatly influenced by its binding to plasma proteins [7]. For instance, such interactions lead to prolonged in vivo half-life, extended therapeutic efficacy, increased solubility, delayed elimination from the body, and decreased toxicity [8]. The degree of plasma protein binding determines the level of bound and free drug fractions, which consequently affect the pharmacokinetic and pharmacodynamic profiles of the drug [9,10]. 7-OH-MTG, together with other kratom alkaloids (MTG and mitraphylline), have demonstrated high plasma protein binding (> 90%), as determined by equilibrium dialysis [11]. Similarly, the opioid fentanyl was also found to strongly interact with plasma transport proteins, with association constants between 105 and 108 M–1 [12]. High plasma protein binding typically suggests a prolonged duration of action because the drug is gradually released into the bloodstream, which can help provide long-term pain relief. Despite this information, the binding of 7-OH-MTG to specific plasma transport proteins is yet to be elucidated in detail.

Human serum albumin (HSA) and α1-acid glycoprotein (AAG) are crucial transporter and storage proteins for most compounds in the circulatory system. HSA is a single, non-glycosylated polypeptide chain of 585 amino acids with a molecular weight of 66.7 kDa. It is the most abundant protein in mammals, constituting nearly 60% of the total plasma protein, and is present at a concentration in the range of 35–50 g/L [13]. HSA is also a valuable biomarker for various medical conditions such as cancer, rheumatoid arthritis, ischemia, and postmenopausal obesity [14,15]. The secondary structure of HSA is mainly composed of α-helices with no β-sheet components [16]. Crystallographic studies have revealed HSA as a globular protein with a shape that resembles the heart that is composed of the homologous domains I, II, and III, with each domain divided into subdomains A and B [15–17]. It primarily binds acidic molecules but can interact with neutral and basic ligands [15]. The major ligand-binding regions of HSA are in the hydrophobic pockets in subdomains IIA, IIIA, and IB, which are referred to as sites I (Sudlow site I), II (Sudlow site II), and III, respectively [13,18].

AAG, also known as orosomucoid, is the major extracellular lipocalin in the blood plasma [19]. Existing as a single glycosylated polypeptide chain of 183 amino acid residues, its five N-linked glycans contribute up to 45% of its total molecular mass of approximately 41 kDa [20]. It comprises eight anti-parallel β-strands linked by four loops arranged into a β-barrel with three flanking α-helices and a central cleft-like ligand-binding pocket. It is negatively

charged at physiological pH due to the presence of sialic acid [16]. As a positive acute-phase protein, its concentration can be elevated severalfold in various medical conditions [15, 19]. AAG primarily binds to basic and neutral compounds, while some acidic compounds can also bind with lower affinities [15, 21]. The F1*S and A genetic variants of AAG are two polymorphic forms of the protein that exhibit differences in selectivity for ligands [22]. The binding pocket of the F1*S variant is broad and has three lobes (I–III), while that of the A variant only has two lobes (I–II) [20, 22].

Molecular docking is a computational technique used to predict the binding mode and affinity of small molecules to the target receptor. It is useful in drug discovery and design as this technique can provide information regarding the interaction of potential drug candidates with their target proteins based on molecular conformations and measurement of binding energies [23]. On the other hand, molecular dynamics (MD) simulations involve computationally simulating the motions and interactions of atoms and molecules over time, providing insights into the dynamic behavior of biological systems [24]. These simulations assess protein-ligand complexes' structural dynamics, flexibility, and energetics, complementing the static snapshots obtained from molecular docking [25]. Together, molecular docking and MD simulations contribute to understanding ligand–protein interactions and aid in the rational design of novel therapeutics.

In this work, we first explored the drug-likeness and pharmacokinetic properties of 7-OH-MTG through ADMET analysis to assess the suitability of the compound as a drug. A combination of molecular docking and MD simulations was then applied to describe the interaction of 7-OH-MTG with HSA and AAG (both F1*S and A variants). The optimized binding orientation of 7-OH-MTG on the proteins and the intermolecular forces involved in the interactions based on structure analyses and docking data were identified. Additionally, the microenvironment, atomic fluctuation, rigidity, and stability of the proteins were studied in comparison to the ligand-bound complexes. These findings will assist in characterizing the binding mechanism of this psychoactive kratom constituent to plasma transporter proteins, which play a critical role in determining its pharmacological profile.

2. Materials and Methods

2.1. Molecular docking analysis.

Molecular modeling was performed using AutoDock 4.2.6 [26] and AutoDockTools 1.5.7 (ADT) [26]. The 3D structures of the proteins were downloaded from the Protein Data Bank (www.rscb.org), while the 3D conformer of 7-OH-MTG (PubChem ID: 44301524) was obtained from PubChem (https://pubchem.ncbi.nlm.nih.gov) in SDF format. The structure of 7-OH-MTG was optimized with the MMFF94 force field using Chem 3D version 22.0.0.22 before being converted into the PDBQT format using OpenBabel version 3.1.1 [27]. For the docking procedure, the proteins were kept rigid while the ligand was allowed torsional freedom. The non-polar hydrogens of the ligand were merged, and the rotatable bonds were defined. Further, polar hydrogens were added, and Kollman united partial atom charges were assigned to the protein atoms. Existing water and ligand molecules were removed from the protein structures as they may affect the docking.

The atomic coordinates of chain A of the HSA crystal structure (PDB ID: 1BM0, 2.5 Å resolution) were used as input for ADT after removing the water molecules. For blind docking, a simulation box (126 × 126 × 126 Å) with a grid space of 0.681 Å was generated

using AutoGrid to cover the entire molecule, centered at coordinates x = 24.149, y = 19.824, and z = 24.290. For site-specific docking, three ligand binding sites at subdomains IIA, IIIA, and IB were defined using grids of 70 × 70 × 70 points with a grid space of 0.375 Å. These grids were centered at coordinates x = 35.26, y = 32.41, and z = 36.46 for site I (subdomain IIA), x = 14.42, y = 23.55, and z = 23.31 for site II (subdomain IIIA), and x = 42.45, y = 24.47, and z = 15.28 for site III (subdomain IB).

As for AAG, the crystal structures of variant F1*S (PDB ID: 3KQ0, 1.8 Å resolution) and variant A (PDB ID: 3APU, 2.1 Å resolution) were used as the docking receptors. The atomic coordinates of chain A of 3APU were used as input for ADT. For the docking, two grid boxes of 126 × 126 × 126 Å centered at x = 21.242, y = −3.094, and z = 2.081 (grid space of 0.408 Å) and x = 11.194, y = 1.306, and z = 29.976 (grid space of 0.708 Å) were prepared for 3KQ0 and 3APU, respectively, encompassing the entire protein structure.

Ligand binding energy was evaluated using the Lamarckian genetic algorithm with local search as the search engine with a total of 1000 runs for random docking (both HSA and AAG) and 100 runs for site-specific docking (HSA only). A population of 150 individuals with 27,000 generations and 250,000 energy evaluations were employed, with the operator weights for the crossover, mutation, and elitism set at 0.8, 0.02, and 1, respectively. For the local search, default parameters were used. Cluster analysis was performed on the docking results using a root-mean-square deviation (RMSD) tolerance of 2.0 Å between structures. For post-docking analysis, the conformation with the strongest binding energy was visualized and analyzed using ADT and UCSF Chimera version 1.17.3 [28]. Predictions of the intermolecular forces involved in the docking interactions were performed using BIOVIA Discovery Studio software v21.1.0.20298 (https://www.3ds.com/).

2.2. Molecular dynamics simulations.

The best conformer from each docking output was used in MD simulations to predict the binding mode and the possible effects of the binding on the conformation of the proteins. The MD simulations were performed using the GROMACS software package version 2022.3 [29]. Topology parameters of HSA and both AAG variants were created using the GROMOS96 43a1 force field [30], while the ligand was built using the Dundee PRODRG server [31].

Each ligand-protein complex was immersed in a cubic box with extended simple point charge (SPC-216) water molecules [32]. The protein was kept at the center and at least 1.0 nm from the edge, employing periodic boundary conditions. After water molecules were added, counter ions were added to the system to preserve electroneutrality. The entire system was composed of the atoms of the protein (HSA: 5843 atoms; AAG variant F1*S: 1872 atoms; AAG variant A: 1913 atoms), the ligand (7-OH-MTG), and Na^+ counter ions (15 for HSA; 7 for AAG variant F1*S; 5 for AAG variant A).

For energy minimization, the steepest descent method (50,000 steps) was used for incompatible contact releases with a cutoff of 1.2 nm for van der Waals and Coulomb forces. To prevent protein position deviation, the simulation was performed using NVT and NPT ensembles. The leap-frog algorithm [33] was used to integrate Newton's second equation of motion with a time step of 2 fs. The protein and ligand were restrained during the NVT and NPT equilibration, with the LINear Constraint Solver (LINCS) holonomic algorithm [34] used to constrain hydrogen bonds. Long-range electrostatic interactions were calculated using the Particle Mesh Ewald (PME) method [35] with a 1.2 nm grid width employing fourth-order cubic interpolation. The short-range electrostatic and van der Waals interactions were

described using the Verlet cutoff scheme with a 1.2 nm cutoff radius and were updated at each time step. Each system was equilibrated for 100 ps at 300 K using a V-rescale (modified Berendsen) thermostat [36], followed by another equilibration for 100 ps at 1 atm using a Parrinello-Rahman barostat [37]. Finally, this was followed by 100 ns MD simulations with a time step of 2 fs for all systems to generate trajectory data for analysis.

The MD trajectories were visualized using VMD version 1.9.4a57 and analyzed using the Xmgrace program (https://plasma-gate.weizmann.ac.il/Grace/). The analysis was performed using various GROMACS inbuilt programs, including root mean square deviation (RMSD), root mean square fluctuation (RMSF), total energy, Rg (Radius of gyration), and solvent-accessible surface area (SASA).

3. Results and Discussion

3.1. Drug-likeness and ADMET properties of 7-OH-MTG.

Before proceeding with preclinical studies, *in silico* prediction of the pharmacokinetic profile of a potential drug is often performed as a quick and simple method to evaluate its therapeutic effectiveness and safety. This study predicted the physicochemical, drug-likeness, and pharmacokinetic properties of 7-OH-MTG using the SwissADME [38] and pkCSM [39] web servers (Table 1).

Table 1. Drug-likeness properties of 7-OH-MTG.

Property	Reference Value	7-OH-MTG
Molecular weight (Da)	< 500	414.49
Log P	≤ 5	2.27
Hydrogen bond donor	≤ 5	1
Hydrogen bond acceptor	< 10	7
Topological polar surface area (Å)	< 140	80.59
Number of rotatable bonds	< 10	6
Molar refractivity (cm^3/mol)	40–130	121.14
Synthetic accessibility	0 ≤ SA ≤ 10	5.21
Lipinski's Rule of Five		Yes
Egan Rule		Yes
Ghose's Filter		Yes
Muegge Rule		Yes
Veber's Rules		Yes
Bioavailability score		0.55

Lipinski's rule of five, which considers a molecule's weight, lipophilicity, and number of hydrogen bond acceptors and donors, is arguably the most widely used set of criteria for determining the suitability of a potential therapeutic agent as an orally administered drug. As shown in Table 1, 7-OH-MTG complied with all these parameters, suggesting that it possesses favorable oral absorption and distribution properties within the body [40]. The total polar surface area (TPSA) is a measure of the surface area of a molecule that is associated with heteroatoms (oxygen, nitrogen, phosphorus) as well as polar hydrogen atoms [41]. 7-OH-MTG has a TPSA value of <140 Å, indicating good intestinal absorption once it enters the body [42]. Furthermore, its number of rotatable bonds and molar refractivity are optimal for sufficient

absorption and bioavailability [24]. Its synthetic accessibility is estimated at 5.21, indicating that it may require particular synthetic processes but is still feasible to produce using available chemical methods. Nevertheless, this is not a major concern since 7-OH-MTG can be produced by simple chemical modification of MTG, the most abundant kratom alkaloid. Moreover, 7-OH-MTG also adheres to several other drug-likeness rules, including those by Egan, Ghose, Muegge, and Veber, with a bioavailability score 0.55.

Table 2 summarizes the main pharmacokinetic properties of 7-OH-MTG. A water solubility of −3.911 might, at first, indicate potential issues with formulation and distribution due to its poor solubility (<1 mg/mL). However, this is unlikely to be a limitation since hydrophobic compounds rely on binding to plasma protein for their circulation in the bloodstream [43], hence the importance of this work. The high percentage of human intestinal absorption (93.5%) suggests a high potential for absorption into systemic circulation upon oral administration, which is beneficial for drug delivery. As a P-glycoprotein substrate, the plasma concentration of 7-OH-MTG may be altered by administering inhibitors or inducers of this efflux pump. The negative BBB and CNS permeability values indicate low permeability across the blood-brain barrier, providing some obstacles to attaining therapeutic concentrations in brain tissues upon oral administration. With regard to metabolism, it is worth pointing out that 7-OH-MTG is predicted to be a substrate for CYP3A4, the most important P450 enzyme that metabolizes xenobiotics.

Further, 7-OH-MTG has a high elimination level, as indicated by its total clearance index of 0.781. As a whole, 7-OH-MTG can be regarded as safe based on the predicted toxicity properties. An LD_{50} value of 2.954 suggests minimal risk of acute toxicity, and it was also unlikely to produce allergic reactions and mutagenic effects.

Table 2. Predicted pharmacokinetic properties of 7-OH-MTG.

Pharmacokinetic property	Parameter	Reference value	7-OH-MTG
Absorption	Water solubility (log mol/L)	High: > −2.0 Moderate: −4.0 to −2.0 Low: < −4.0	−3.911
	Human intestinal absorption	High: > 80% Moderate: 30–80% Low: < 30%	93.503
	P-glycoprotein substrate		Yes
Distribution	BBB permeability (log BB)	High: > 0.3 Low: < −1.0	−0.206
	CNS permeability (log PS)	High: > −2 Low: < −3	−2.47
Metabolism	CYP2D6 substrate		No
	CYP3A4 substrate		Yes
	CYP1A2 inhibitor		No
	CYP2C19 inhibitor		No
	CYP2C9 inhibitor		No
	CYP2D6 inhibitor		No
	CYP3A4 inhibitor		No
Excretion	Total clearance (log ml/min/kg)	High: > 0.5 Moderate: 0–0.5 Low: < 0	0.781
Toxicity	Ames toxicity		No
	Oral rat acute toxicity, LD50 (mol/kg)	High: < 2.5 Moderate: 2.5–5.0 Low: > 5.0	2.954
	Skin sensitization		No

3.2. Molecular docking of 7-OH-MTG to HAS.

Molecular docking analysis was performed using the AutoDock software package version 4.2.6 to predict the binding site of 7-OH-MTG on HSA. Blind docking of 7-OH MTG to HSA with 1000 production runs was first performed prior to site-specific docking to the major drug binding sites of HSA with 100 production runs for each site.

Cluster analysis of the blind docking of 7-OH-MTG to HSA (Figure 2A) resulted in 187 multimember conformational clusters from 1000 runs. Interestingly, the most stable clusters (binding energy < −9 kcal mol^{-1}) were dominated by 7-OH-MTG conformations that were docked to subdomain IB (determined based on the identity of the amino acids), which contains drug site III. Likewise, site-specific docking results shown in Figure 2B indicate the preference of 7-OH-MTG to bind to site III of HSA based on binding energy and cluster population, followed by site I and site II.

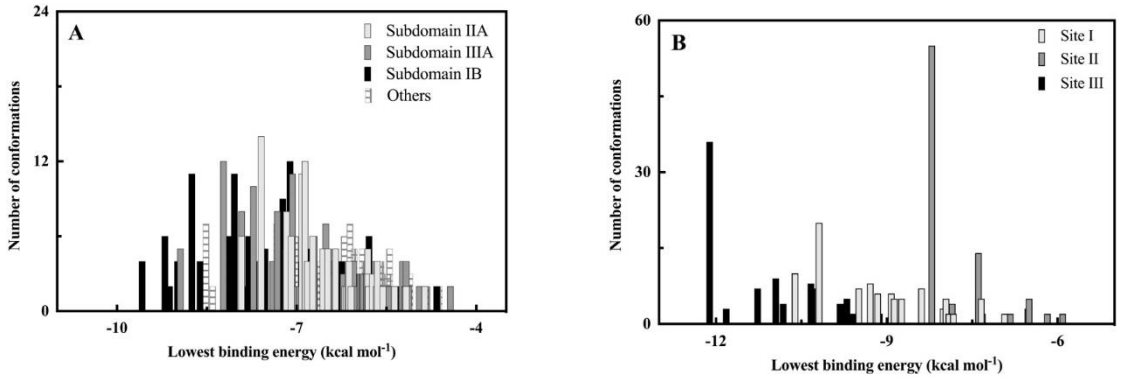

Figure 2. Cluster analysis of the docking of 7-OH-MTG to HSA (PDB ID: 1BM0). **(A)** blind docking with 1000 runs; **(B)** site-specific docking to sites I, II, and III of HSA with 100 runs for each site.

Figure 3A shows the best docking conformation (lowest binding energy) of 7-OH-MTG upon blind docking to HSA, which was at binding site III with the lowest binding energy of −9.58 kcal mol^{-1}. The ligand was embedded deep into the binding pocket, with only its anisole ring remaining at the surface. Drug site III of HSA is known to be the binding site for approximately 60 compounds with varying structural characteristics [44]. It is the primary binding site for endogenous compounds such as bilirubin (and related molecules including biliverdin and hemin) as well as drugs such as lidocaine and fusidic acid [18, 44]. Additionally, it serves as the secondary binding site for azapropazone, indomethacin, and 2,3,5-triiodobenzoic acid [13, 45]. Interestingly, sites III and I were demonstrated to be allosterically coupled, explaining the potential of heme to reduce the affinity of site I ligands, including anti-HIV drugs, to HSA [18].

Structure analysis of 7-OH-MTG using the ChemAxon (*Chemicalize*) program revealed that only a minority of the total population of 7-OH-MTG exists in the charged form at physiological pH, comprising 45.2% (Figures S1 and S2). Therefore, ionic interactions are not expected to be significant in binding this compound and plasma proteins. On the other hand, the logD value of 7-OH-MTG, which measures the compound's lipophilicity, was 2.49 at pH 7.4 (Figure S3), strongly indicating the involvement of hydrophobic interactions in the complexation of 7-OH-MTG with proteins. Furthermore, the analysis indicates that 7-OH-MTG possesses six hydrogen bond acceptors and a single hydrogen bond donor, supporting the potential formation of hydrogen bonds with proteins.

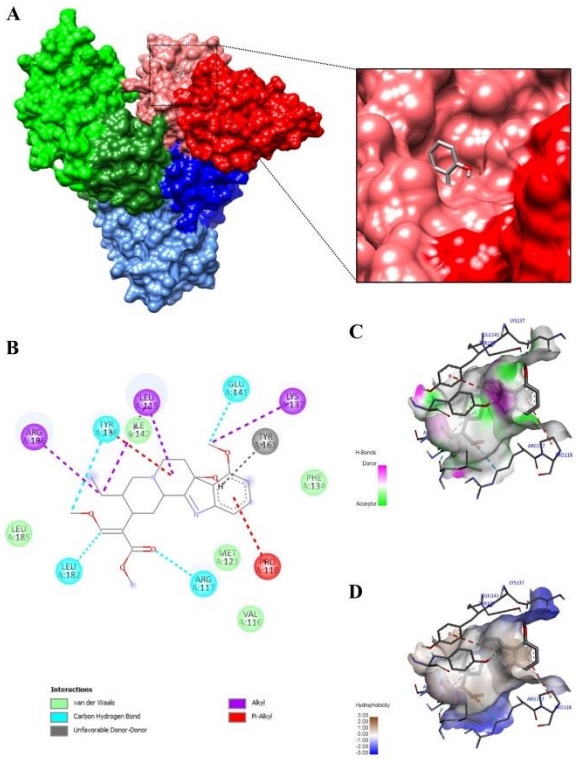

Figure 3. (A) Molecular surface representation of the docking of 7-OH-MTG on HSA (PDB ID: 1BM0), showing the binding orientation of the lowest docking energy conformation of 7-OH-MTG (−9.58 kcal/mol) after 1000 runs. The HSA subdomains are colored as follows: red for IA, light red for IB, blue for IIA, light blue for IIB, green for IIIA, and light green for IIIB. Schematic representations of **(B)** the intermolecular forces involved and the participating amino acid residues; **(C)** hydrogen bonding surface; **(D)** surface hydrophobicity at the docking site of 7-OH-MTG on HSA.

The intermolecular forces involved in forming the 7-OH-MTG−HSA complex at site III are shown in Figure 3B (details are presented in Table S1). Although no conventional hydrogen bonds were found in the interactions, four carbon-hydrogen bonds were predicted for the 7-OH-MTG−HSA complex, mediated by Leu-182, Arg-117, Glu-141, and Tyr-138. The spatial regions of the residues acting as donors (pink) and acceptors (green) of hydrogen bonding with 7-OH-MTG are indicated in Figure 3C. In addition, 7-OH-MTG formed strong interactions with the binding site on HSA through hydrophobic (alkyl and pi-alkyl) and van der Waals forces. The hydrophobicity profile of the area surrounding the docked 7-OH-MTG (Figure 3D) is color-coded, with the hydrophilic region represented in blue (negative scores) and the hydrophobic region in brown (positive scores). Van der Waals forces also played a role in the HSA complexation with 7-OH-MTG involving the residues Ile-142, Phe-134, Met-123, Val-116, and Leu-185. On the other hand, an unfavorable donor-donor interaction involving Tyr-161 and 7-OH-MTG (Figure 4B) was also present, contributing to the lesser stability of the 7-OH-MTG−HSA complex compared to its interaction with AAG.

3.3. Molecular docking of 7-OH-MTG to AAG.

In studying the interactions of 7-OH-MTG with AAG, blind docking (1000 runs) using crystal structures of variants F1*S and A of human AAG was performed. As shown in Figure 4, the conformational clusters with the lowest binding energy for the complexation of 7-OH-MTG with AAG variant F1*S (−9.95 kcal mol^{-1}) and A (−10.44 kcal mol^{-1}) were not the highest populated cluster. Nevertheless, the binding energy of these clusters was considerably

lower compared to that of the highest populated docking clusters of the 7-OH-MTG to both AAG variants.

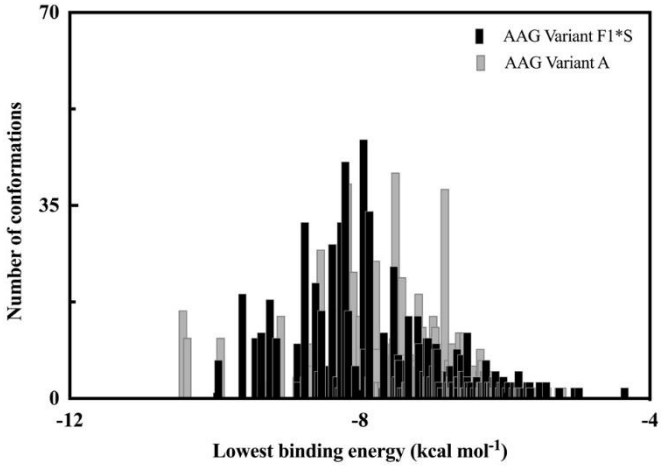

Figure 4. Cluster analysis of the docking of 7-OH-MTG to AAG variants F1*S (PDB ID: 3KQ0) and A (PDB ID: 3APU) after 1000 docking runs for each variant.

The differential binding behavior of the ligand towards the F1*S and A variants can be attributed to the variance between their amino acid compositions (which differ by 20 out of the total 183 residues), resulting in unique topology structures and drug binding selectivity [20, 22]. As an example, dipyridamole molecules have a greater affinity towards the F1*S variant, whereas tricyclic compounds featuring two benzene rings exhibit a preference for the A variant [20]. Despite AAG possessing more than seven potential binding sites, only the central binding pocket of the protein has a noteworthy therapeutic significance, exhibiting a high affinity towards drugs [46,47]. The central binding pocket of the variant F1*S is relatively large and comprises three lobes (I–III). Lobe I is a major non-polar sub-compartment of the binding cavity and acts as a hydrophobic drug-binding chamber. In contrast, lobes II and III are smaller and negatively charged due to the presence of acidic amino acid residues (Glu64 in lobe II and Asp115 in lobe III) [20, 48]. In contrast, the narrower central ligand-binding pocket of the A variant consists of only two lobes: the main hydrophobic lobe I, flanked by the smaller lobe II [48, 49]. Studies have also shown that the interaction of several compounds, including cimetidine, chlorpromazine, disopyramide, mianserin, nortriptyline, and desipramine with AAG involves overlap of the different lobes of the binding pocket, irrespective of the AAG variant [20, 49].

3.3.1. AAG variant F1*S.

Figure 5 depicts the lowest binding energy conformation of 7-OH-MTG (−9.95 kcal mol^{-1}) on variant F1*S of AAG. The ligand was docked to the central binding pocket of the protein and was primarily localized at lobe I (Figure 5A). Interestingly, the interaction (details in Table S2) involved a conventional hydrogen bond, with the hydroxyl group at C7 of 7-OH-MTG acting as a hydrogen bond donor to form a bond with Ser-125 at an interatomic distance of 2.49 Å (Figures 5B and 5C). Additionally, 7-OH-MTG formed carbon-hydrogen bonds with the protein involving Tyr-37 and Arg-90. Various hydrophobic forces (pi-sigma, pi-alkyl, alkyl) played major roles in binding 7-OH-MTG to AAG, emphasizing the hydrophobic surroundings of the bound ligand (Figure 5D). The contribution of van der Waals forces in stabilizing the complexation was also significant, as indicated by the participation of a high number of amino acid residues shown in Figure 5B.

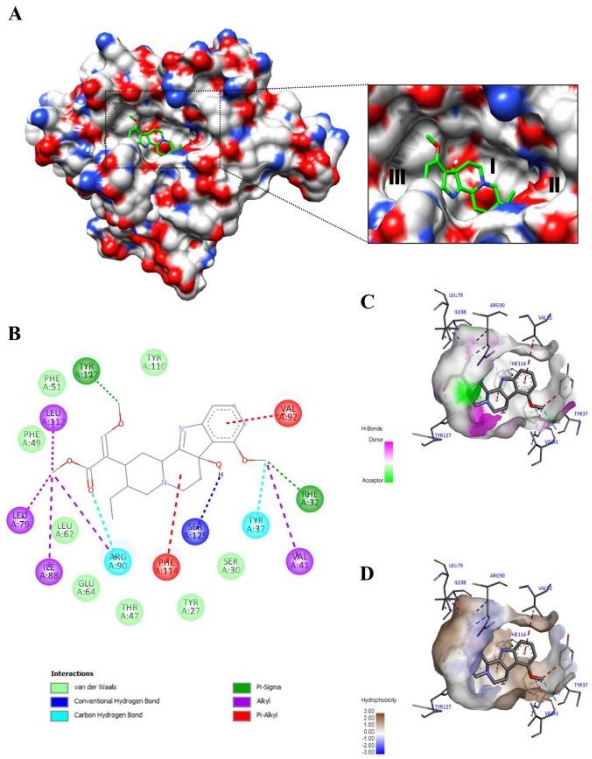

Figure 5. (A) Molecular surface representation of the docking of 7-OH-MTG on variant F1*S of AAG (PDB ID: 3KQ0), showing the binding orientation of the lowest docking energy conformation of 7-OH-MTG (−9.95 kcal/mol) after 1000 runs. The protein is colored according to the CPK color scheme. The enlarged view of the binding site shows lobes I-III of the protein. Schematic representations of **(B)** the intermolecular forces involved and the participating amino acid residues; **(C)** hydrogen bonding surface; **(D)** surface hydrophobicity at the docking site of 7-OH-MTG on the protein.

3.3.2. AAG variant A.

Analogous to its binding to the variant F1*S of AAG, 7-OH-MTG was also found to dock within the central cavity of variant A of the protein (Figure 6A), with a binding energy of −10.44 kcal mol^{-1}. The intermolecular forces responsible for stabilizing the ligand-protein complex are shown in Figure 6B (details in Table S3). The contribution of hydrogen bonding in this interaction is evident from the formation of two hydrogen bonds mediated by Gln-66 (2.03 Å) and Arg-90 (3.10 Å) (Figures 6B and 6C). The relatively weaker carbon-hydrogen bonds are also implicated in the complexation. Unsurprisingly, the non-polar nature of 7-OH-MTG facilitated the formation of several hydrophobic bonds, such as pi-alkyl, pi-sigma, and alkyl interactions with the protein, as depicted in Figures 6B and 6D. The multiple instances of pi-sigma interactions involving charge transfer between electron-rich aromatic residues (Tyr-27, Tyr-37, and Phe-112) and the electron-deficient moieties of 7-OH-MTG are seen to strongly contribute towards the stability of the compound at the binding site. Moreover, van der Waals forces were also significantly featured, with almost the entirety of 7-OH-MTG being encompassed by amino acid residues participating in these forces (Figure 6B).

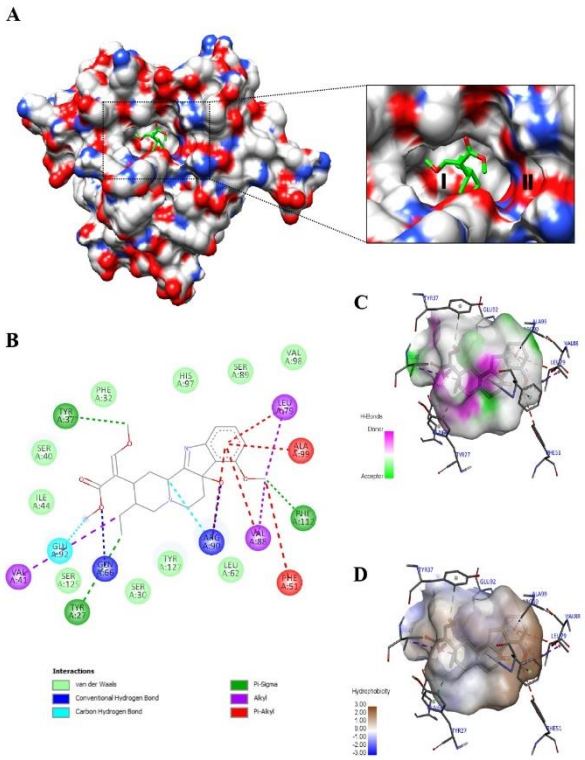

Figure 6. (A) Molecular surface representation of the docking of 7-OH-MTG on variant A of AAG (PDB ID: 3APU), showing the binding orientation of the lowest docking energy conformation of 7-OH-MTG (−10.44 kcal/mol) after 1000 runs. The protein is colored according to the CPK color scheme. The enlarged view of the binding site shows lobes I and II of the protein. Schematic representations of **(B)** the intermolecular forces involved and the participating amino acid residues; **(C)** hydrogen bonding surface; **(D)** surface hydrophobicity at the docking site of 7-OH-MTG on the protein.

3.4. Validation of docking procedure.

To validate the accuracy and reliability of the molecular docking procedure, we redocked the originally crystallized ligand to the protein using the structure of AAG variant A (PDB ID: 3APU) as our model. Figure 7A compares the crystallized and redocked poses of the ligand tetraethylene glycol on the protein. As can be seen, the redocked ligand attached to the protein at the same location as the crystallized ligand. Furthermore, the ligand RMSD between the two poses was 1.885 Å, indicating a high similarity between structures [50]. Moreover, the amino acid residues interacting with the ligand's two structures were identified and found to be almost identical (Figures 7B and 7C), thus reaffirming the robustness of the docking protocol.

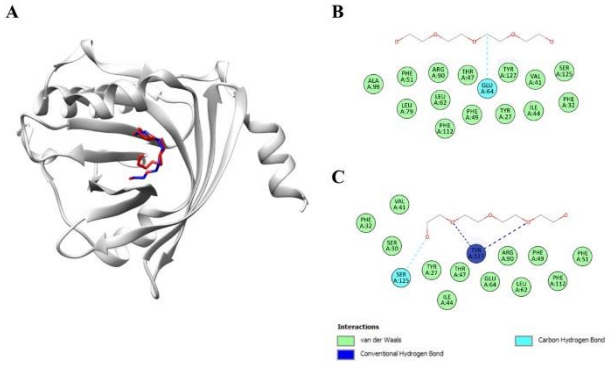

Figure 7. (A) Comparison of the crystallized (blue) and redocked (red) poses of the ligand tetraethylene glycol with AAG variant A (PDB ID: 3APU). Interaction of amino acid residues with the **(B)** crystallized; **(C)** redocked ligand.

3.5. Molecular dynamics (MD) simulations.

Molecular simulation studies, which compute the behavior of a system as a function of time, have emerged as a powerful tool for understanding the interaction between proteins and ligands to predict how conformational changes occur to achieve the lowest free energy state [25]. Exploration of the conformational space of ligand-protein complexes involving 7-OH-MTG, HSA, and both variants of AAG at the atomic level by MD helps in understanding the energetically favorable states, the transition between states, as well as structural stability and flexibility of the molecular systems. Therefore, analyses of root-mean-square deviation (RMSD), root-mean-square fluctuation (RMSF), total energy, radius of gyration (Rg), and solvent-accessible surface area (SASA) fluctuations were performed for each molecular system.

3.5.1. Protein stability and flexibility.

RMSD, a quantitative measure of the average distance between corresponding atoms in different structures, can be used as an indicator of the stability of ligand-protein complexes. The relative decrease in RMSD values suggests a less pronounced protein conformational change, which reflects the increase in its rigidity and stability, with values in the range 0.1–0.3 nm accepted as reasonable for conformational perturbations of globular proteins [51]. To assess the structural stability of HSA and AAG, RMSD values were obtained from MD simulations of the native proteins and their complexes with 7-OH-MTG. According to Figure 8A, HSA and its complexes with 7-OH-MTG achieved an equilibrium phase without any major shifts in RMSD. The RMSD value of native HSA stabilized at ~0.47 nm from about 40 ns until the end of run time, in line with values from previous reports [52,53]. The RMSD values of the 7-OH-MTG–HSA complex showed only a slight increase compared to free protein, suggesting that the introduction of the ligand did not induce major changes to the structural stability and flexibility of HSA.

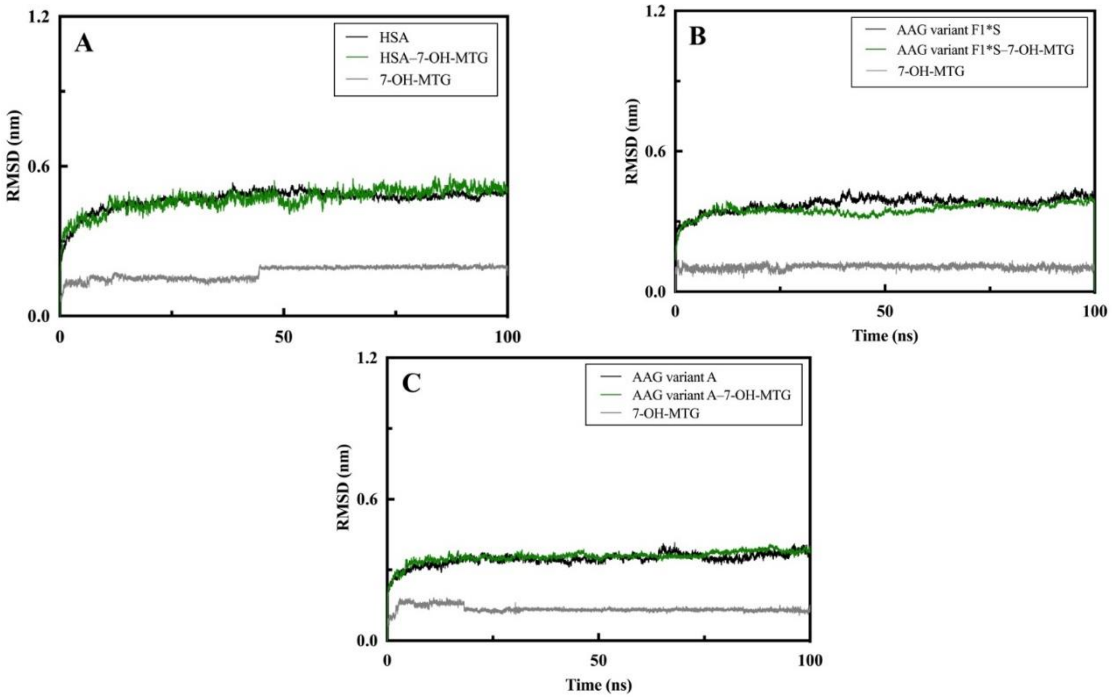

Figure 8. RMSD plots of **(A)** HAS; **(B)** AAG variant F1*S; **(C)** AAG variant A and their complexes with 7-OH-MTG against simulation time.

With regard to AAG, the RMSD values for both variants F1*S and A in their native states were between 0.33 nm and 0.37 nm after 10 ns of simulation time. For the variant FI*S, its complex with 7-OH-MTG exhibited consistently lower RMSD values compared to the native protein, albeit by only a small degree (Figure 8B). However, there were no marked differences in RMSD value before and after the complexation of the A variant with 7-OH-MTG (Figure 8C). The bound 7-OH-MTG showed low RMSD values of around 0.15 nm, indicating its relative stability at the binding site and the consistency of its interaction with the proteins. The small fluctuations in RMSD value at the beginning of the simulations were possibly due to the system's startup and setup adjustments. Overall, the interaction of 7-OH-MTG with AAG (especially variant F1*S) appears more stable than that with HSA. Nevertheless, all complexes were stable throughout the 100 ns simulations with few conformational transitions, demonstrating the structural similarity of the native and bound states of the proteins.

The total energy in MD simulations refers to the sum of kinetic and potential energies, representing the dynamic state of the system. Understanding this concept helps analyze the stability, thermodynamic properties, and physical behavior of the molecular system. Based on the results shown in Figure 9, the total energy of the various 7-OH-MTG–protein complexes was nearly uniform throughout the simulation period. Hence, it can be concluded that these complexes were stable, supporting the RMSD results.

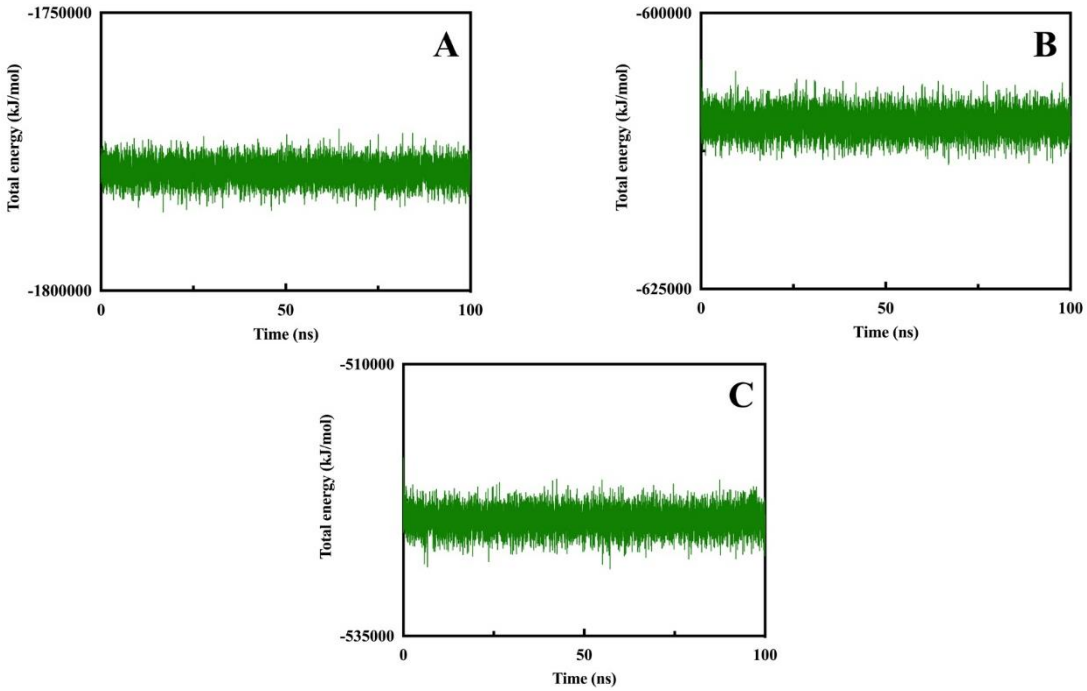

Figure 9. Time evolution of the total energy of the complex between 7-OH-MTG and **(A)** HAS; **(B)** AAG variant F1*S; **(C)** AAG variant A.

RMSF, a measure of the average deviation of residues of a protein over time, is another metric commonly used to assess proteins' flexibility and conformational transitions. The comparative RMSF of HSA and AAG (variants F1*S and A) residues in the free and ligand-bound states are represented in Figure 10. For the most part, the 7-OH-MTG–HSA complex exhibited similar RMSF values compared to native HSA, except for select residues that make up subdomain IB of the protein, wherein drug site III is located (Figure 10AI). Specifically, the binding of 7-OH-MTG to HSA induced a slight increase in the RMSF values of several residues at the binding site, most notably Leu-115, Arg-117, and Pro-118 (Figure 10AII). The higher-

than-average RMSF of certain residues corresponded to the loop regions that are typically more flexible than other sections of the protein [54]. RMSF analysis of the ligand-bound AAG structures showed nearly identical fluctuations as the free protein, as illustrated in Figures 10BI and 10CI for variants F1*S and A, respectively.

In contrast to HSA, the atomic fluctuations of variant F1*S residues involved in the interaction with 7-OH-MTG within the central binding pocket are lower compared to the native protein (Figure 10BII). The same trend was also observed for variant A of AAG, involving Tyr-37, Phe-51, Leu-79, Arg-90, Glu-92, and Phe-112 (Figure 10CII). These simulation data support the formation of stable complexations between 7-OH-MTG and both variants of AAG, with increased rigidity of the protein microenvironment in the vicinity of the binding site [46]. Overall, the binding pocket of both proteins demonstrated adaptation to effectively accommodate the ligands, involving structural rearrangements that affected the local flexibility of the docking site, consistent with previous reports [55,56].

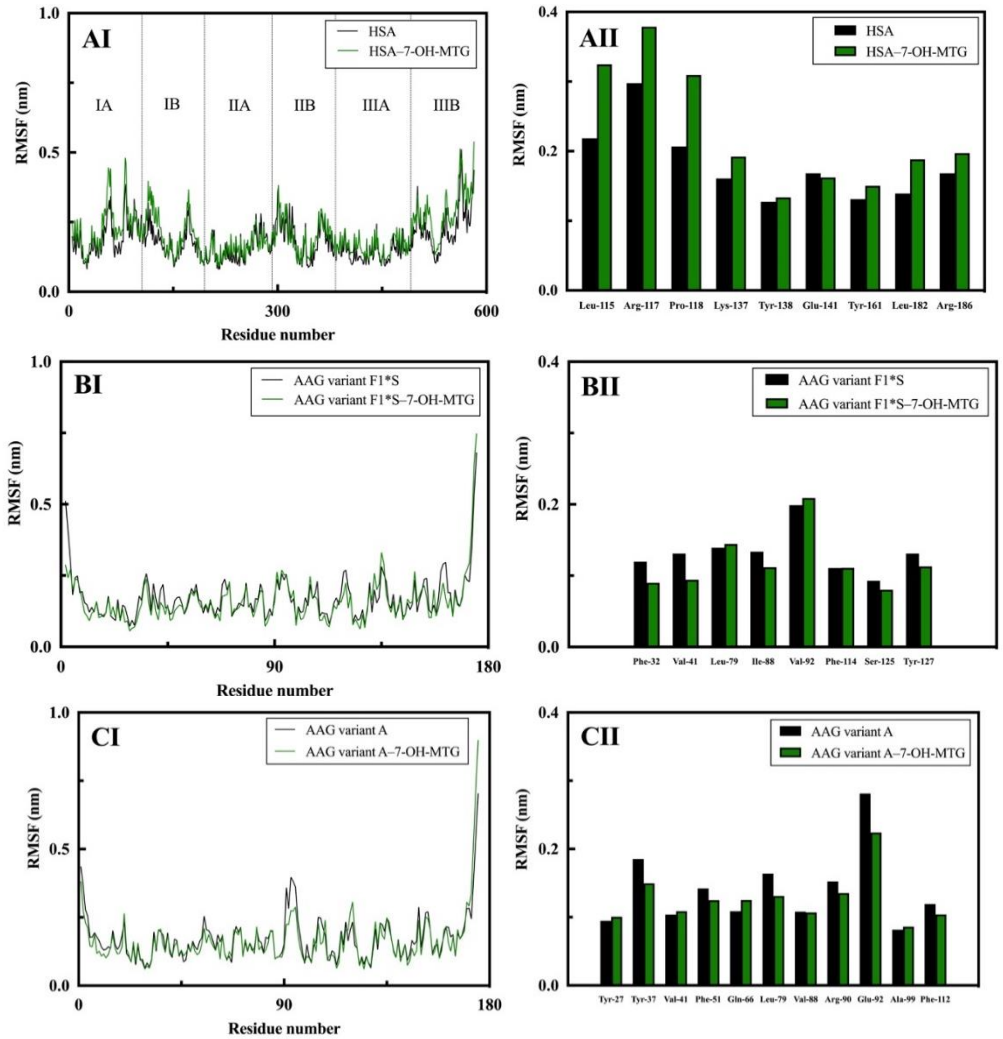

Figure 10. (AI–CI) RMSF values of HSA and AAG (variants F1*S and A) residues in the absence and presence of 7-OH-MTG. (AII–CII) Comparative RMSF profiles of HSA and AAG (variants F1*S and A) residues at the binding site before and after the docking of 7-OH-MTG.

3.5.2. Protein compactness and folding.

The radius of gyration (Rg), defined as the distribution of protein atoms around the rotation axis, is often used to characterize the dynamic trajectory of proteins to assess their compactness [58]. The closer distribution of mass to the axis is reflected by small Rg values,

indicating a more compactly folded system [49]. In this study, the structural compactness of HSA and AAG upon the binding of 7-OH-MTG was estimated based on the Rg value of each system. The average Rg values of free HSA and the 7-OH-MTG–HSA complex were 2.57 and 2.58 nm, respectively, during the last 60 ns of the simulation (Figure 11A). As a comparison, the experimentally determined Rg value of native HSA in aqueous solution was 2.74 nm based on neutron scattering experiments [59].

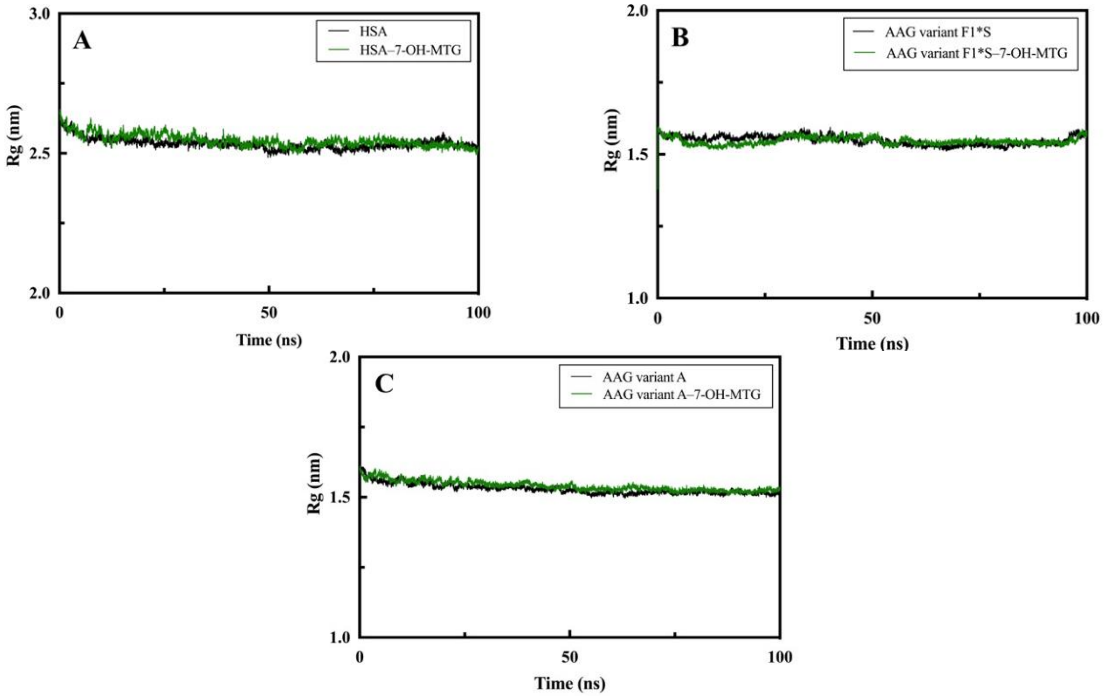

Figure 11. Time evolution of the radius of gyration of **(A)** HAS; **(B)** AAG variant F1*S; **(C)** AAG variant A in the absence and presence of 7-OH-MTG.

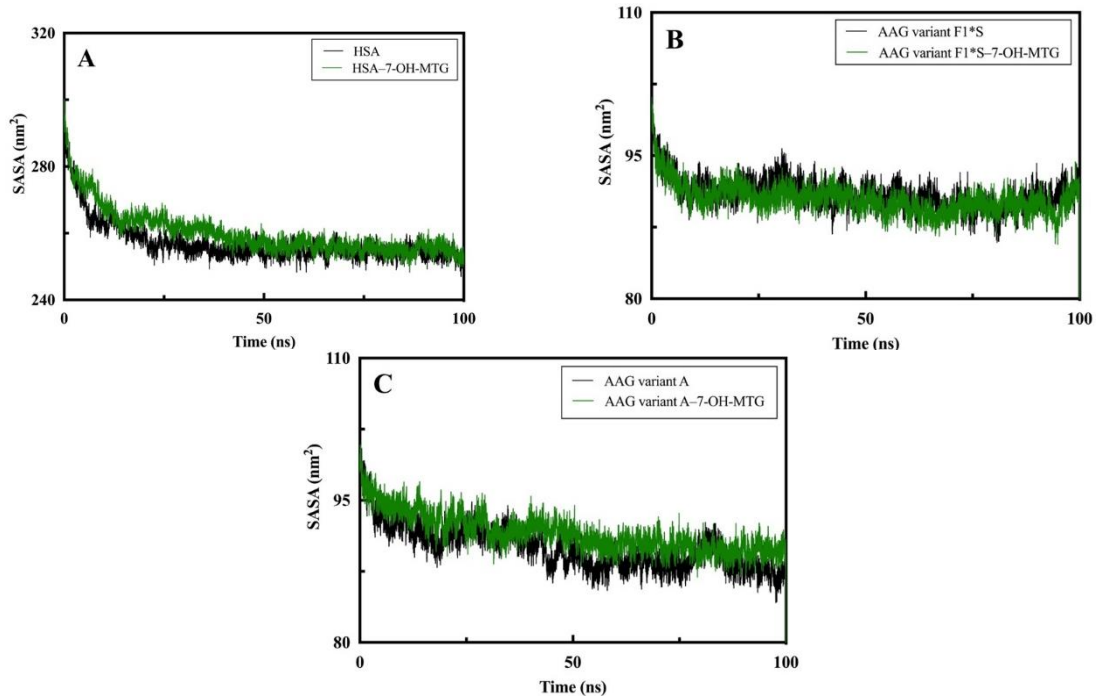

Figure 12. SASA plots of **(A)** HAS; **(B)** AAG variant F1*S; **(C)** AAG variant A in the absence and presence of 7-OH-MTG as a function of time.

Nevertheless, it should be noted that the changes in Rg observed in our simulations were relatively minor. As smaller proteins, both F1*S (Figure 11B) and A (Figure 11C) of

AAG exhibited average Rg values of ~1.55 nm upon reaching equilibrium. However, the presence of 7-OH-MTG did not significantly alter the Rg of both AAG variants, probably due to the already compact nature of the protein structures.

The solvent-accessible surface area (SASA) of proteins, an essential indicator of protein folding and stability, is a measure of the exposure of amino acid residues to the surrounding solvent. As shown in Figure 12A, the SASA values of HSA and its complex with 7-OH-MTG were almost identical post the 70 nm mark. Similarly, there were substantial overlaps in the SASA fluctuations of AAG variants F1*S (Figure 12B) and A (Figure 12C) in the absence and presence of the ligands, suggesting no significant alteration in the folding of these proteins upon binding to 7-OH-MTG.

4. Conclusions

This work investigates the interaction of 7-OH-MTG, a potent psychoactive compound found in kratom, with human transport proteins. Based on ADMET assessments, 7-OH-MTG appears suitable as an oral drug with favorable physicochemical and pharmacokinetic features. Molecular docking experiments strongly suggested site III, located in subdomain IB, as the preferred binding site of 7-OH-MTG on HSA. In the case of AAG, 7-OH-MTG was preferentially docked to the central binding pocket of both variants F1*S and A of the protein. Involvement of hydrogen bonds, hydrophobic interaction, and van der Waals forces were identified in the complexation of 7-OH-MTG with the plasma proteins. In general, the structure of AAG was more favorably adapted for binding with 7-OH-MTG. Nonetheless, all ligand-protein complexes showed stable trajectories, as indicated by low RMSD and RMSF values. The compactness and folding of both proteins upon 7-OH-MTG binding are also comparable to their native forms based on the minimal fluctuations in Rg and SASA values. This study helps in understanding the interaction of the psychoactive 7-OH-MTG with the major human transport proteins and may prove beneficial in the future development of therapeutic agents derived from kratom. Nevertheless, investigating the interaction of 7-OH-MTG with other transport proteins and extending MD simulations under various physiological conditions will further deepen our understanding of its pharmacological properties and potential applications. Further, validating these results through in vitro and in vivo studies and performing comprehensive toxicity and safety profiling is essential.

Funding

This work was financially supported by the Fundamental Research Grant Scheme from the Ministry of Higher Education Malaysia (FRGS/1/2019/STG04/UKM/02/6).

Acknowledgments

Declared none.

Conflicts of Interest

The authors declare no conflict of interest.

References

1. Hossain, R.; Sultana, A.; Nuinoon, M.; Noonong, K.; Tangpong, J.; Hossain, K. H.; Rahman, M. A. A critical review of the neuropharmacological effects of kratom: An insight from the functional array of identified natural compounds. *Molecules* **2023**, 28, 7372, https://doi.org/10.3390/molecules28217372.
2. Ahmad, I.; Prabowo, W. C.; Arifuddin, M.; Fadraersada, J.; Indriyanti, N.; Herman, H.; Purwoko, R. Y.; Nainu, F.; Rahmadi, A.; Paramita, S.; Kuncoro, H.; Mita, N.; Narsa, A. C.; Prasetya, F.; Ibrahim, A.; Rijai, L.; Alam, G.; Mun'im, A.; Dej-adisai, S. *Mitragyna* species as pharmacological agents: from abuse to promising pharmaceutical products. *Life* **2022**, *12*, 193, https://doi.org/10.3390/life12020193.
3. Karunakaran, T.; Ngew, K. Z.; Zailan, A. A. D.; Mian Jong, V. Y.; Abu Bakar, M. H. The chemical and pharmacological properties of mitragynine and its diastereomers: An insight review. *Front. Pharmacol*. **2022**, *13*, 1–11, https://doi.org/10.3389/fphar.2022.805986.
4. Vicknasingam, B.; Narayanan, S.; Beng, G. T.; Mansor, S. M. The informal use of ketum (*Mitragyna speciosa*) for opioid withdrawal in the northern states of Peninsular Malaysia and implications for drug substitution therapy. *Int. J. Drug Policy* **2010**, *21*, 283–288, https://doi.org/10.1016/j.drugpo.2009.12.003.
5. Obeng, S.; Wilkerson, J. L.; León, F.; Reeves, M. E.; Restrepo, L. F.; Gamez-Jimenez, L. R.; Patel, A.; Pennington, A. E.; Taylor, V. A.; Ho, N. P.; Braun, T.; Fortner, J. D.; Crowley, M. L.; Williamson, M. R.; Pallares, V. L. C.; Mottinelli, M.; Lopera-Londoño, C.; McCurdy, C. R.; McMahon, L. R.; Hiranita, T. Pharmacological comparison of mitragynine and 7-hydroxymitragynine: In vitro affinity and efficacy for μ-opioid receptor and opioid-like behavioral effects in rats. *J. Pharmacol. Exp. Ther*. **2021**, *376*, 410–427, https://doi.org/10.1124/jpet.120.000189.
6. Berthold, E. C.; Kamble, S. H.; Raju, K. S.; Kuntz, M. A.; Senetra, A. S.; Mottinelli, M.; León, F.; Restrepo, L. F.; Patel, A.; Ho, N. P.; Hiranita, T.; Sharma, A.; McMahon, L. R.; McCurdy, C. R. The lack of contribution of 7-hydroxymitragynine to the antinociceptive effects of mitragynine in mice: A pharmacokinetic and pharmacodynamic study. *Drug Metab. Dispos.* **2022**, *50*, 158–167, https://doi.org/10.1124/dmd.121.000640.
7. Bakar, K. A.; Lam, S. D.; Sidek, H. M.; Feroz, S. R. Characterization of the interaction of diosgenin with human serum albumin and α1-acid glycoprotein using biophysical and bioinformatic tools. *J. Mol. Liq*. **2020**, *306*, 112865, https://doi.org/10.1016/j.molliq.2020.112865.
8. Yamasaki, K.; Chuang, V. T. G.; Maruyama, T.; Otagiri, M. Albumin–drug interaction and its clinical implication. *Biochim. Biophys. Acta - Gen. Subj.* **2013**, *1830*, 5435–5443, https://doi.org/10.1016/j.bbagen.2013.05.005.
9. Bakar, K. A.; Feroz, S. R. A critical view on the analysis of fluorescence quenching data for determining ligand–protein binding affinity. *Spectrochim. Acta Part A Mol. Biomol. Spectrosc*. **2019**, *223*, 117337, https://doi.org/10.1016/j.saa.2019.117337.
10. Deb, P.K.; Al-Attraqchi, O.; Prasad, M.R.; Tekade, R.K. Chapter 11 - Protein and Tissue Binding: Implication on Pharmacokinetic Parameters. In Dosage Form Design Considerations, Tekade, R.K., Ed.; Academic Press: **2018**; pp. 371-399, https://doi.org/10.1016/B978-0-12-814423-7.00011-3.
11. Manda, V.; Avula, B.; Ali, Z.; Khan, I.; Walker, L.; Khan, S. Evaluation of in vitro absorption, distribution, metabolism, and excretion (ADME) properties of mitragynine, 7-hydroxymitragynine, and mitraphylline. *Planta Medica* **2014**, *80*, 568–576, https://doi.org/10.1055/s-0034-1368444.
12. Bednarek, R.; Luzak, B.; Golański, J.; Boncler, M. Interactions of fentanyl with blood platelets and plasma proteins: platelet sensitivity to prasugrel metabolite is not affected by fentanyl under in vitro conditions. *Pharmacol. Res.* **2023**, *75*, 423–441, https://doi.org/10.1007/s43440-023-00447-7.
13. Rimac, H.; Dufour, C.; Debeljak, Ž.; Zorc, B.; Bojić, M. Warfarin and flavonoids do not share the same binding region in binding to the IIA subdomain of human serum albumin. *Molecules* **2017**, *22*, 1153, https://doi.org/10.3390/molecules22071153.
14. Fanali, G.; di Masi, A.; Trezza, V.; Marino, M.; Fasano, M.; Ascenzi, P. Human serum albumin: from bench to bedside. *Mol. Aspects Med.* **2012**, *33*, 209–290, https://doi.org/10.1016/j.mam.2011.12.002.
15. Ascenzi, P.; Fanali, G.; Fasano, M.; Pallottini, V.; Trezza, V. Clinical relevance of drug binding to plasma proteins. *J. Mol. Struct.* **2014**, *1077*, 4–13, https://doi.org/10.1016/j.molstruc.2013.09.053.
16. Bteich, M. An overview of albumin and alpha-1-acid glycoprotein main characteristics: highlighting the roles of amino acids in binding kinetics and molecular interactions. *Heliyon* **2019**, *5*, e02879, https://doi.org/10.1016/j.heliyon.2019.e02879.

17. Kaur, M.; Bhattacharya, M.; Maity, B. Deciphering conformational changes in human serum albumin induced by bile salts using spectroscopic and molecular modeling approaches. *J. Mol. Liq.* **2023**, *390*, 123026, https://doi.org/10.1016/j.molliq.2023.123026.
18. Lemli, B.; Lomozová, Z.; Huber, T.; Lukács, A.; Poór, M. Effects of Heme Site (FA1) Ligands Bilirubin, Biliverdin, Hemin, and Methyl Orange on the Albumin Binding of Site I Marker Warfarin: Complex Allosteric Interactions. *Int. J. Mol. Sci.* **2022**, *23*, 14007, https://doi.org/10.3390/ijms232214007.
19. Ruiz, M. Into the labyrinth of the lipocalin α1-acid glycoprotein. *Front. Physiol.* **2021**, *12*, 686251, https://doi.org/10.3389/fphys.2021.686251.
20. Schönfeld, D. L.; Ravelli, R. B. G.; Mueller, U.; Skerra, A. The 1.8-å crystal structure of α1-acid glycoprotein (orosomucoid) solved by UV RIP reveals the broad drug-binding activity of this human plasma lipocalin. *J. Mol. Biol.* **2008**, *384*, 393–405, https://doi.org/10.1016/j.jmb.2008.09.020.
21. Huang, Z.; Ung, T. Effect of alpha-1-acid glycoprotein binding on pharmacokinetics and pharmacodynamics. *Curr. Drug Metab.* **2013**, *14*, 226–238, https://doi.org/10.2174/1389200211314020011.
22. Nishi, K.; Ono, T.; Nakamura, T.; Fukunaga, N.; Izumi, M.; Watanabe, H.; Suenaga, A.; Maruyama, T.; Yamagata, Y.; Curry, S.; Otagiri, M. Structural insights into differences in drug-binding selectivity between two forms of human α1-acid glycoprotein genetic variants, the A and F1*S forms. *J. Biol. Chem.* **2011**, *286*, 14427–14434, https://doi.org/10.1074/jbc.M110.208926.
23. Bouamrane, S.; Khaldan, A.; Hajji, H.; El-mernissi, R.; Alaqarbeh, M.; Alsakhen, N.; Maghat, H.; Ajana, M. A.; Sbai, A.; Bouachrine, M.; Lakhlifi, T. In silico identification of 1,2,4-triazoles as potential *Candida Albicans* inhibitors using 3D-QSAR, molecular docking, molecular dynamics simulations, and ADMET profiling. *Molecular Diversity*, **2023**, *27*, 2111–2132, https://doi.org/10.1007/s11030-022-10546-x.
24. Khaldan, A.; Bouamrane, S.; El-mernissi, R.; Alaqarbeh, M.; Hajji, H.; Alsakhen, N.; Maghat, H.; Ajana, M. A.; Sbai, A.; Bouachrine, M.; Lakhlifi, T. Computational study of quinoline-based thiadiazole compounds as potential antileishmanial inhibitors. *New J. Chem.* **2022**, *46*, 17554–17576, https://doi.org/10.1039/D2NJ03253H.
25. Salo-Ahen, O. M. H.; Alanko, I.; Bhadane, R.; Bonvin, A. M. J. J.; Honorato, R. V.; Hossain, S.; Juffer, A. H.; Kabedev, A.; Lahtela-Kakkonen, M.; Larsen, A. S.; Lescrinier, E.; Marimuthu, P.; Mirza, M. U.; Mustafa, G.; Nunes-Alves, A.; Pantsar, T.; Saadabadi, A.; Singaravelu, K.; Vanmeert, M. Molecular dynamics simulations in drug discovery and pharmaceutical development. *Processes*. **2020**, *9*, 71, https://doi.org/10.3390/pr9010071.
26. Morris, G. M.; Huey, R.; Lindstrom, W.; Sanner, M. F.; Belew, R. K.; Goodsell, D. S.; Olson, A. J. AutoDock4 and AutoDockTools4: Automated docking with selective receptor flexibility. *J. Comput. Chem.* **2009**, *30*, 2785–279, https://doi.org/10.1002/jcc.21256.
27. O'Boyle, N. M.; Banck, M.; James, C. A.; Morley, C.; Vandermeersch, T.; Hutchison, G. R. Open babel: an open chemical toolbox. *J. Cheminform.* **2011**, *3*, 33. https://doi.org/10.1186/1758-2946-3-33.
28. Pettersen, E. F.; Goddard, T. D.; Huang, C. C.; Couch, G. S.; Greenblatt, D. M.; Meng, E. C.; Ferrin, T. E. UCSF Chimera - A visualization system for exploratory research and analysis. *J. Comput. Chem.* **2004**, *25*, 1605–1612, https://doi.org/10.1002/jcc.20084.
29. Van Der Spoel, D.; Lindahl, E.; Hess, B.; Groenhof, G.; Mark, A. E.; Berendsen, H. J. C. GROMACS: fast, flexible, and free. *J. Comput. Chem.* **2005**, *26*, 1701–1718, https://doi.org/10.1002/jcc.20291.
30. Pol-Fachin, L.; Fernandes, C. L.; Verli, H. GROMOS96 43a1 Performance on the Characterization of glycoprotein conformational ensembles through molecular dynamics simulations. *Carbohydr. Res.* **2009**, *344*, 491–500, https://doi.org/10.1016/j.carres.2008.12.025.
31. Schüttelkopf, A. W.; van Aalten, D. M. F. PRODRG: a tool for high-throughput crystallography of protein–ligand complexes. *Acta Crystallogr. Sect. D Biol. Crystallogr.* **2004**, *60*, 1355–1363, https://doi.org/10.1107/S0907444904011679.
32. van der Spoel, D.; van Maaren, P. J.; Berendsen, H. J. C. A systematic study of water models for molecular simulation: derivation of water models optimized for use with a reaction field. *J. Chem. Phys.* **1998**, *108*, 10220–10230, https://doi.org/10.1063/1.476482.
33. Van Gunsteren, W. F.; Berendsen, H. J. C. A leap-frog algorithm for stochastic dynamics. *Mol. Simul.* **1988**, *1*, 173–185, https://doi.org/10.1080/08927028808080941.
34. Hess, B.; Bekker, H.; Berendsen, H. J. C.; Fraaije, J. G. E. M. LINCS: A linear constraint solver for molecular simulations. *J. Comput. Chem.* **1997**, *18* 1463–1472, https://doi.org/10.1002/(SICI)1096-987X(199709)18:12<1463::AID-JCC4>3.0.CO;2-H.

35. Darden, T.; York, D.; Pedersen, L.; Darden, T.; York, D.; Pedersen, L. Particle mesh ewald: An *N* log (*N*) method for ewald sums in large systems. *J. Chem. Phys.* **1993**, *98*, 10089-10092, https://doi.org/10.1063/1.464397.
36. Bussi, G.; Donadio, D.; Parrinello, M. Canonical sampling through velocity rescaling. *J. Chem. Phys*. **2007**, *126*, 014101, https://doi.org/10.1063/1.2408420.
37. Parrinello, M.; Rahman, A. Polymorphic transitions in single crystals: A new molecular dynamics method. *J. Appl. Phys*. **1981**, *52*, 7182–7190, https://doi.org/10.1063/1.328693.
38. Daina, A.; Michielin, O.; Zoete, V. SwissADME: a free web tool to evaluate pharmacokinetics, drug-likeness and medicinal chemistry friendliness of small molecules. *Sci. Rep.* **2017**, *7*, 42717, https://doi.org/10.1038/srep42717.
39. Pires, D. E. V.; Blundell, T. L.; Ascher, D. B. pkCSM: Predicting small-molecule pharmacokinetic and toxicity properties using graph-based signatures. *J. Med. Chem.* **2015**, *58*, 4066–4072. https://doi.org/10.1021/acs.jmedchem.5b00104
40. Benet, L. Z.; Hosey, C. M.; Ursu, O.; Oprea, T. I. BDDCS, the Rule of 5 and drugability. *Adv. Drug Deliv. Rev*. **2016**, *101*, 89–98, https://doi.org/10.1016/j.addr.2016.05.007.
41. Prasanna, S., & Doerksen, R. Topological polar surface area: A useful descriptor in 2D-QSAR. *Curr. Med. Chem.* **2009**, *16*, 21–41, https://doi.org/10.2174/092986709787002817.
42. Maximo da Silva, M.; Comin, M.; Santos Duarte, T.; Foglio, M.; de Carvalho, J.; do Carmo Vieira, M.; Nazari Formagio, A. Synthesis, antiproliferative activity and molecular properties predictions of galloyl derivatives. *Molecules* **2015**, *20*, 5360–5373, https://doi.org/10.3390/molecules20045360.
43. Tayyab, S.; Feroz, S.R. Chapter Nine - Serum albumin: clinical significance of drug binding and development as drug delivery vehicle. In Advances in Protein Chemistry and Structural Biology, Donev, R., Ed.; Academic Press: **2021**; Volume 123, pp. 193-218, https://doi.org/10.1016/bs.apcsb.2020.08.003.
44. Zsila, F. Subdomain IB Is the Third Major Drug Binding Region of Human Serum Albumin: Toward the Three-Sites Model. *Mol. Pharm*. **2013**, *10*, 1668–1682, https://doi.org/10.1021/mp400027q.
45. Ghuman, J.; Zunszain, P. A.; Petitpas, I.; Bhattacharya, A. A.; Otagiri, M.; Curry, S. Structural basis of the drug-binding specificity of human serum albumin. *J. Mol. Biol*. **2005**, *353*, 38–52, https://doi.org/10.1016/j.jmb.2005.07.075.
46. Israili, Z. H.; Dayton, P. G. Human alpha-1-glycoprotein and its interactions with drugs. *Drug Metab. Rev.* **2001**, *33*, 161–235, https://doi.org/10.1081/DMR-100104402.
47. Maharaj, A. R.; Gonzalez, D.; Cohen-Wolkowiez, M.; Hornik, C. P.; Edginton, A. N. Improving pediatric protein binding estimates: an evaluation of α1-acid glycoprotein maturation in healthy and infected subjects. *Clin. Pharmacokinet*. **2018**, *57*, 577–589, https://doi.org/10.1007/s40262-017-0576-7.
48. Zsila, F. Quorum sensing-associated bacterial phenazines are potential ligands of human α1-acid glycoprotein. *J. Mol. Recognit.* **2023**, *36*, e3027, https://doi.org/10.1002/jmr.3027.
49. Huang, J. X.; Cooper, M. A.; Baker, M. A.; Azad, M. A. K.; Nation, R. L.; Li, J.; Velkov, T. Drug-binding energetics of human α-1-acid glycoprotein assessed by isothermal titration calorimetry and molecular docking simulations. *J. Mol. Recognit*. **2012**, *25*, 642–656, https://doi.org/10.1002/jmr.2221.
50. Daoui, O.; Elkhattabi, S.; Chtita, S.; Elkhalabi, R.; Zgou, H.; Benjelloun, A. T. QSAR, molecular docking and ADMET properties in silico studies of novel 4,5,6,7-tetrahydrobenzo[D]-thiazol-2-Yl derivatives derived from dimedone as potent anti-tumor agents through inhibition of C-Met receptor tyrosine kinase. *Heliyon*. **2021**, *7*, e07463, https://doi.org/10.1016/j.heliyon.2021.e07463.
51. Naik, R. S.; Pawar, S. K.; Tandel, R. D.; J, S. Insights into the mechanism of interaction of a thrombin inhibitor, dabigatran etexilate with human serum albumin and influence of β-cyclodextrin on binding: spectroscopic and computational approach. *J. Mol. Liq.* **2018**, *251*, 119–127, https://doi.org/10.1016/j.molliq.2017.12.056.
52. Ali, M. S.; Muthukumaran, J.; Jain, M.; Tariq, M.; Al-Lohedan, H. A.; Al-Sanea, A. S. S. Detailed experimental and in silico investigation of indomethacin binding with human serum albumin considering primary and secondary binding sites. *Molecules* **2023**, *28*, 2979, https://doi.org/10.3390/molecules28072979.
53. Shamsi, A.; Shahwan, M.; Khan, M.S.; Alhumaydhi, F.A.; Alsagaby, S.A.; Al Abdulmonem, W.; Abdullaev, B.; Yadav, D.K. Mechanistic Insight into Binding of Huperzine A with Human Serum Albumin: Computational and Spectroscopic Approaches. *Molecules* **2022**, *27*, 797, https://doi.org/10.3390/molecules27030797.

54. Asngari, N. J. M.; Bakar, K. A.; Feroz, S. R.; Razak, F. A.; Halim, A. A. A. Interaction mechanism of a cysteine protease inhibitor, odanacatib, with human serum albumin: *in vitro* and bioinformatics studies. *Biophys. Chem.* **2024**, *305*, 107140, https://doi.org/10.1016/j.bpc.2023.107140.
55. Dubey, S.; Kallubai, M.; Sarkar, A.; Subramanyam, R. Elucidating the active interaction mechanism of phytochemicals withanolide and withanoside derivatives with human serum albumin. *PLoS One* **2018**, *13*, 1–17, https://doi.org/10.1371/journal.pone.0200053.
56. Gokara, M.; Malavath, T.; Kalangi, S. K.; Reddana, P.; Subramanyam, R. Unraveling the binding mechanism of asiatic acid with human serum albumin and its biological implications. *J. Biomol. Struct. Dyn.* **2014**, *32*, 1290–1302, https://doi.org/10.1080/07391102.2013.817953.
57. Yeggoni, D. P.; Rachamallu, A.; Kallubai, M.; Subramanyam, R. Cytotoxicity and comparative binding mechanism of piperine with human serum albumin and α-1-acid glycoprotein. *J. Biomol. Struct. Dyn.* **2015**, 33, 1336–1351, https://doi.org/10.1080/07391102.2014.947326.
58. Lobanov, M. Y.; Bogatyreva, N. S.; Galzitskaya, O. V. Radius of gyration as an indicator of protein structure compactness. *Mol. Biol.* **2008**, *42*, 623–628, https://doi.org/10.1134/S0026893308040195.
59. Kiselev, M.A.; Gryzunov, I.A.; Dobretsov, G.E.; Komarova, M.N. Size of a human serum albumin molecule in solution. *Biofizika* **2001**, *46*, 423–427.

Supplementary materials

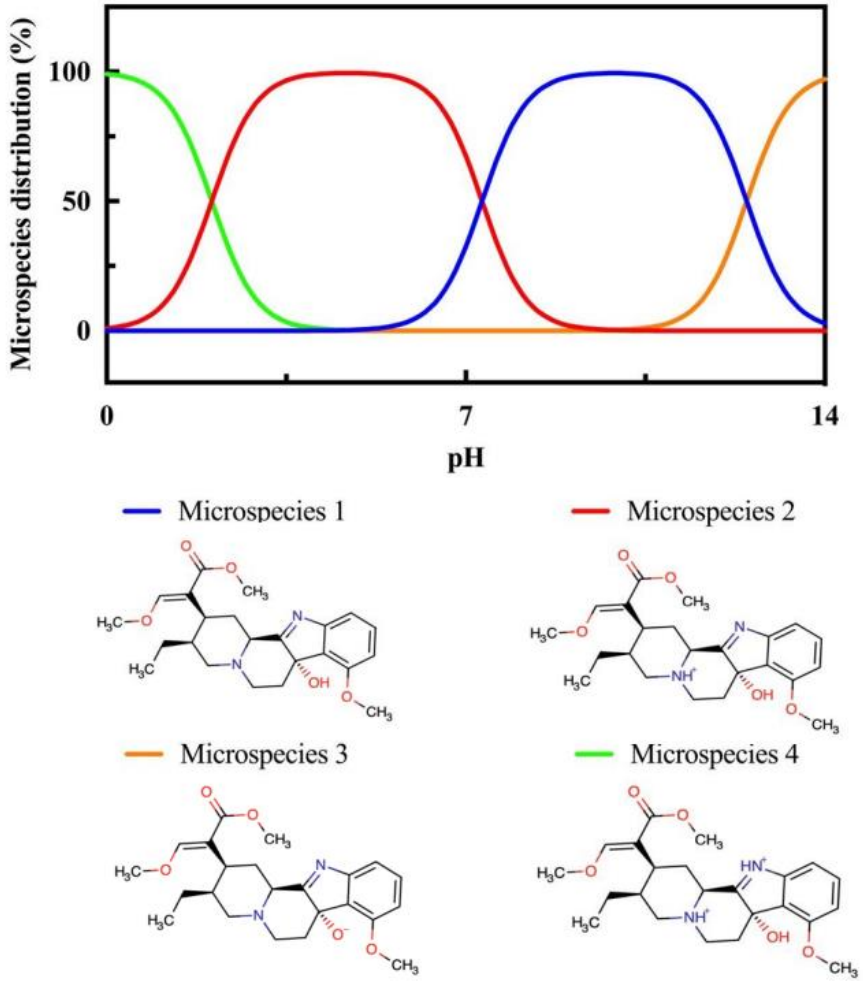

Figure S1. Microspecies distribution of 7-OH-MTG over the pH range 0−14.

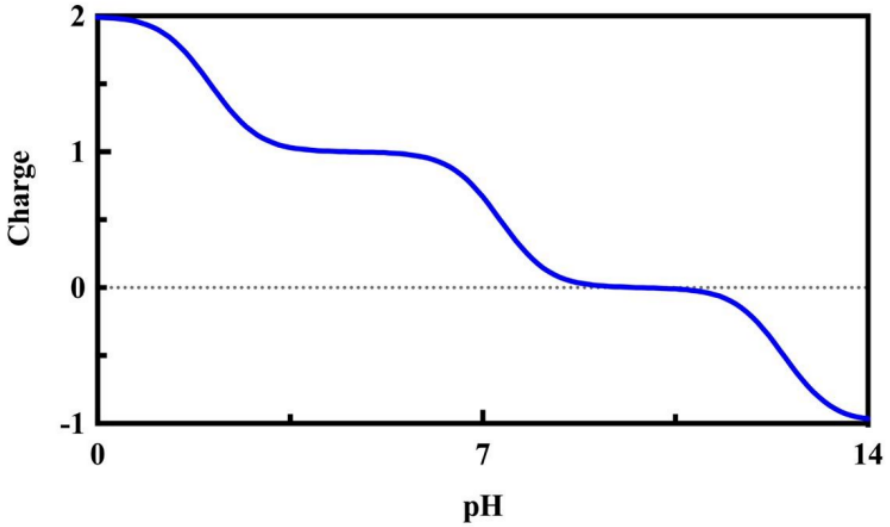

Figure S2. Net charge of 7-OH-MTG over the pH range 0−14. The net charge of 7-OH-MTG at the physiological pH 7.4 is 0.45.

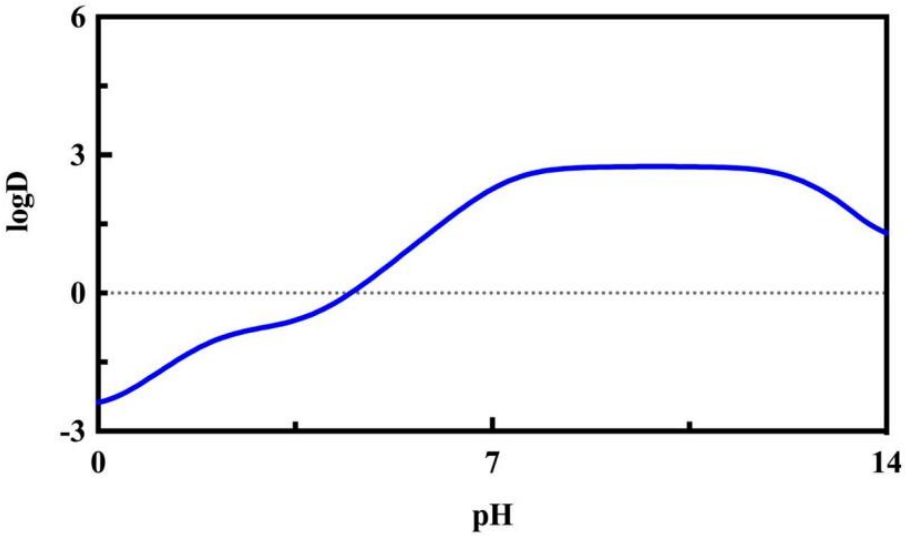

Figure S3. The logD values of 7-OH-MTG over the pH range 0−14.

Table S1. Intermolecular interactions involved in the complexation of 7-OH-MTG with HSA.

Complex	Type of interaction		Interaction point	Distance (Å)
HSA + 7-OH-MTG	Unfavorable	Unfavorable donor-donor	A:TYR161:HH - : LIG:H	2.12
	Hydrogen bond	Carbon hydrogen bond	LIG:C - A:TYR138:OH	3.59
			LIG:C - A:LEU182:O	2.76
			A:ARG117:CD - : LIG:O	3.18
			LIG:C - A:GLU141:OE2	3.06
	Hydrophobic interaction	Pi-alkyl	LIG - A:PRO118	5.12
			A:TYR138 - : LIG	5.28
		Akyl	LIG:C - A:LYS137	3.46
			LIG:C - A:LEU115	5.15
			LIG:C - A:ARG186	4.61
			A:LEU115 - : LIG:C	4.65

Table S2. Intermolecular interactions involved in the complexation of 7-OH-MTG with AAG variant F1*S.

Complex	Type of interaction		Interaction point	Distance (Å)
AAG variant F1*S + 7-OH-MTG	Hydrogen bond	Conventional hydrogen bond	LIG:H - A:SER125:OG	2.49
		Carbon hydrogen bond	A:ARG90:CD - : LIG:O	3.22
			LIG:C - A:TYR37:O	3.53
	Hydrophobic interaction	Pi-sigma	LIG:C - A:PHE32	3.81
			LIG:C - A:TYR127	3.41
		Pi-alkyl	A:PHE114 - : LIG	5.37
			A:TYR37 - : LIG:C	4.70
			LIG - A:VAL92	5.15
		Alkyl	LIG:C - A:ARG90	4.42
			LIG:C - A:VAL41	4.39
			LIG:C - A:LEU79	4.39
			LIG:C - A:LEU112	5.23
			LIG:C - A:ILE88	4.40

Table S3. Intermolecular interactions involved in the complexation of 7-OH-MTG with AAG variant A.

Complex	Type of interaction		Interaction point	Distance (Å)
AAG variant A + 7-OH-MTG	Hydrogen bond	Conventional hydrogen bond	A:GLN66:HE22 - : LIG:O	2.03
			A:ARG90:NH1 - : LIG:O	3.10
		Carbon hydrogen bond	LIG:C - A:GLU92:OE2	3.42
			LIG:C - A:ARG90:NH1	3.29
			A:ARG90:CD - : LIG:O	3.06
	Hydrophobic interaction	Pi-sigma	LIG:C - A:TYR37	3.95
			LIG:C - A:PHE112	3.60
			LIG:C - A:TYR27	3.78
		Pi-alkyl	A:PHE51 - : LIG:C	4.95
			LIG - A:ARG90	4.05
			LIG - A:VAL88	5.43
			LIG - A:LEU79	5.32
			LIG - A:ALA99	4.46
		Alkyl	LIG:C - A:VAL41	4.97
			LIG:C - A:VAL88	4.70
			LIG:C - A:LEU79	4.73